



Active nematic ratchet in asymmetric obstacle arrays

Cody D. Schimming ^{*}, C. J. O. Reichhardt , and C. Reichhardt

Theoretical Division and Center for Nonlinear Studies, Los Alamos National Laboratory, Los Alamos, New Mexico 87545, USA



(Received 19 March 2024; accepted 3 May 2024; published 3 June 2024)

We numerically investigate the effect of an asymmetric periodic obstacle array in a two-dimensional active nematic. We find that activity in conjunction with the asymmetry leads to a ratchet effect or unidirectional flow of the fluid along the asymmetry direction. The directional flow is still present even in the active turbulent phase when the gap between obstacles is sufficiently small. We demonstrate that the dynamics of the topological defects transition from flow mirroring to smectic-like as the gap between obstacles is made smaller, and explain this transition in terms of the pinning of negative winding number defects between obstacles. This also leads to a nonmonotonic ratchet effect magnitude as a function of obstacle size, so that there is an optimal obstacle size for ratcheting at fixed activity.

DOI: [10.1103/PhysRevE.109.064602](https://doi.org/10.1103/PhysRevE.109.064602)

I. INTRODUCTION

Active nematics are anisotropic fluids that exhibit local orientational order and generate macroscopic flows from microscopic forces [1,2]. In large, unconfined systems these flows are typically chaotic, leading to a phase dubbed “active turbulence” [3–6]. Additionally, orientational order in the nematic allows the existence of topological defects, which may spontaneously nucleate in the active turbulence phase and act as sources for the flow [7–11]. In addition to the inherent interest in chaotic flows and defect dynamics in active nematic turbulence, much recent activity has focused on controlling the flows for potential technological applications such as microfluidic devices and flow-based logic gates [12]. Proposed flow control methods include modifying the boundary geometry, employing spatially varying activity, applying external fields, and altering substrate properties [13–20]. There has also been experimental work on the interaction of active nematics with fabricated obstacle arrays [21,22], where defect pinning was observed.

A ratchet effect can be used to control flows in systems coupled to an asymmetric substrate under external ac driving or flashing of the substrate [23–26]. Ratchet effects have been demonstrated for colloidal particles [27,28] and superconducting vortices [29,30], where ac driving results in a net unidirectional flow of particles. In active matter systems coupled to asymmetric substrates, ratchet effects can arise without external driving due to the activity [31,32]. Particle-based active matter ratchets have been studied for biological systems such as swimming bacteria [33] as well as active colloids [32,34]. An open question is whether ratchet effects also occur for active nematics coupled to an asymmetric substrate, and if so, how the fluid flow and topological defect dynamics would be modified.

Here, we numerically study a two-dimensional active nematic interacting with a periodic array of obstacles of triangular shape, creating an array with a clearly defined asymmetry axis. Topological defects, which are known to generate flows [2,11], spontaneously appear in the system out of geometrical necessity due to the shape of the obstacles. We show that when the gap between the asymmetric obstacles is sufficiently small, an active nematic ratchet effect occurs in the form of unidirectional flow along the asymmetry axis, something that does not occur for an array of symmetric obstacles [35]. Ratcheting effects have been observed for rotational flows in active nematics interacting with asymmetric inclusions and boundaries [36,37], but, to our knowledge, this is the first realization of a translational active nematic ratchet. We demonstrate that the ratchet effect is robust across a wide range of obstacle gap sizes and activity levels. By tuning the gap size, a transition in the defect dynamics occurs, and the flow speed is optimized at the transition point.

II. ACTIVE NEMATIC MODEL

We model a two-dimensional active nematic using a well-established nematohydrodynamics model in terms of the tensor order parameter $\mathbf{Q} = S[\mathbf{n} \otimes \mathbf{n} - (1/2)\mathbf{I}]$, where S is the local degree of orientational order and the director, \mathbf{n} , gives the local orientation of the nematic [2,38]. The evolution equation for \mathbf{Q} is given by

$$\frac{\partial \mathbf{Q}}{\partial t} + (\mathbf{v} \cdot \nabla) \mathbf{Q} - \mathbf{S} = -\frac{1}{\gamma} \frac{\delta F}{\delta \mathbf{Q}} \quad (1)$$

where \mathbf{v} is the fluid velocity, γ is a rotational viscosity, F is the free energy, and

$$\begin{aligned} \mathbf{S} = & (\lambda \mathbf{E} + \boldsymbol{\Omega})(\mathbf{Q} + \frac{1}{2}\mathbf{I}) + (\mathbf{Q} + \frac{1}{2}\mathbf{I})(\lambda \mathbf{E} - \boldsymbol{\Omega}) \\ & - 2\lambda(\mathbf{Q} + \frac{1}{2}\mathbf{I})(\nabla \mathbf{v} : \mathbf{Q}) \end{aligned} \quad (2)$$

is a generalized tensor advection [39]. In Eq. (2), $\mathbf{E} = (\nabla \mathbf{v} + \nabla \mathbf{v}^T)/2$ is the strain rate tensor, $\boldsymbol{\Omega} = (\nabla \mathbf{v} - \nabla \mathbf{v}^T)/2$ is the

^{*}cschim@lanl.gov

rotation rate tensor, and λ is a dimensionless parameter that depends on the geometry of the nematogen and characterizes whether a liquid crystal is flow aligning or tumbling in shear flow. The free energy is given by

$$F = \int (A|\mathbf{Q}|^2 + C|\mathbf{Q}|^4 + L|\nabla\mathbf{Q}|^2) d\mathbf{r}, \quad (3)$$

where A and C are phenomenological parameters and L is the elastic constant.

The fluid velocity is generated from active stresses given by inhomogeneities in the nematic, and is computed from the Stokes equation:

$$\eta\nabla^2\mathbf{v} = \nabla p + \alpha\nabla \cdot \mathbf{Q}, \quad (4)$$

where η is the fluid viscosity, p is the fluid pressure, and α is the strength of active forces, called the activity. We also assume the fluid is incompressible and enforce the constraint $\nabla \cdot \mathbf{v} = 0$.

To put the equations in a dimensionless form, we scale lengths by the nematic correlation length and times by the nematic relaxation time:

$$\tilde{\mathbf{r}} = \frac{\mathbf{r}}{\xi}, \quad \tilde{t} = \frac{t}{\tau}, \quad \xi = \sqrt{\frac{\varepsilon L}{C}}, \quad \tau = \frac{\gamma}{C\xi^2}, \quad (5)$$

where ε is a dimensionless parameter that controls the size of defects. The free energy is scaled by $C\xi^2$ and Eq. (4) may be multiplied by ξ/C to yield a dimensionless equation for the velocity. This gives the dimensionless quantities

$$\tilde{F} = \frac{F}{C\xi^2}, \quad \tilde{A} = \frac{A}{C}, \quad \tilde{p} = \frac{p\tau}{\eta}, \quad \tilde{\alpha} = \frac{\alpha\tau}{\eta}. \quad (6)$$

The nondimensionalization leaves $\tilde{\alpha}$, the dimensionless activity, as the only parameter in Eq. (4).

The active nematic model considered here is associated with three length scales that interact with the confining lengths scales considered in this study. The nematic correlation length ξ is the length over which nematic distortions occur and sets the scale at which all other lengths are compared in this study. The radius of defects ξ_d is set by the parameter ε and is fixed in this work to be $\xi_d \approx \xi$. Finally, the active length scale, $\xi_a = \sqrt{L/\alpha}$ is the length at which active forces perturb the nematic. It is inversely related to defect density in the active turbulent phase [40] and in dimensionless units it is given by $\tilde{\xi}_a = \sqrt{1/\varepsilon\tilde{\alpha}}$. In the following sections, the tildes are omitted for brevity and all quantities given will be in dimensionless units.

III. COMPUTATIONAL METHOD

We numerically solve Eqs. (1) and (4) to simulate active nematic behavior. To do this, we first write \mathbf{Q} in a basis for traceless, symmetric matrices,

$$\mathbf{Q} = \begin{pmatrix} q_1 & q_2 \\ q_2 & -q_1 \end{pmatrix}, \quad (7)$$

and rewrite Eq. (1) in terms of q_1 and q_2 . Eqs. (1) and (4) are then written in weak form and the pressure is used as a Lagrange multiplier to impose the incompressibility condition, $\nabla \cdot \mathbf{v} = 0$. We use the MATLAB/C++ package TIGER [41] to generate a mesh that consists of a square lattice of

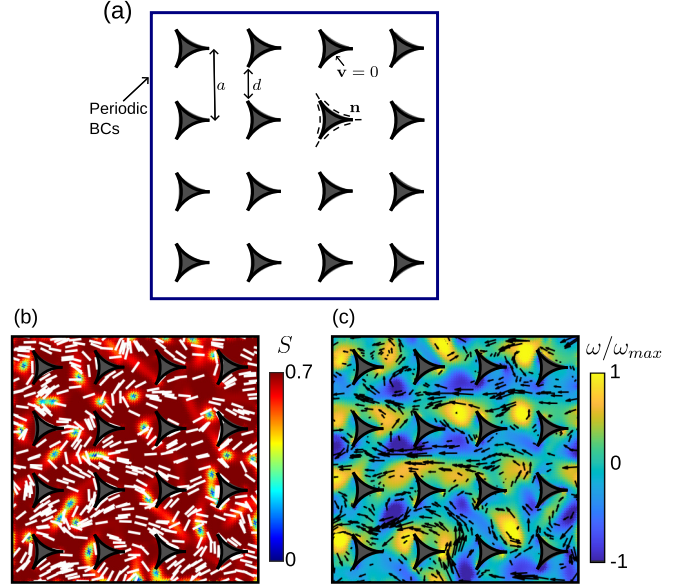


FIG. 1. (a) Schematic of the computational domain with a periodic array of triangular obstacles. (b) Time snapshot of the nematic configuration. The color represents the scalar order parameter S while the white lines represent the director \mathbf{n} . (c) Time snapshot of the vorticity and velocity. The color represents the vorticity while the black lines represent the flow field.

concave triangular obstacles, shown in Fig. 1(a). The triangular obstacles are generated from the arcs of three circles in contact with each other. The number of vertices in each mesh ranges from 18 021 to 19 453 depending on the size of the obstacles. The average distance between vertices is ~ 0.5 . The MATLAB/C++ package FELICITY [42] is then used to generate the finite element matrices from the weak form of Eqs. (1) and (4) on the mesh. The time evolution of \mathbf{Q} is solved using a backward-Euler method with time step $\delta t = 0.5$.

The only model parameter we vary in this study is the activity α . We fix $A = -1/2$ so the passive liquid crystal is in the nematic phase with $S_N = \sqrt{1/2}$, where S_N is the scalar order parameter that minimizes the free energy. We fix $\varepsilon = 4$ which corresponds to a defect radius $\xi_d \approx 1$ and $\lambda = 1$ which corresponds to a flow aligning nematic with Leslie angle $\theta_L \approx 0.33$ [43].

We employ periodic boundary conditions on the outer boundaries of the domain while the boundaries of the fixed obstacles are given Dirichlet conditions such that $S = S_N$, $\mathbf{n} = \mathbf{T}$, where \mathbf{T} is the local tangent vector to the boundary curve, and $\mathbf{v} = 0$. The director \mathbf{n} at the cusp of the obstacles is modified so that it transitions continuously from one side of the cusp to the other. This is occasionally required since \mathbf{T} at the cusps may jump discontinuously due to the finite resolution of the mesh. After ensuring continuity of the director we do not observe any “artificial” defects at the cusps of the obstacles which may arise due to discontinuities in the director field. We initialize the system with a random director field except at the fixed boundaries. We simulate in the range of 1000 to 2000 time steps to allow each system to reach a dynamical steady state, which is defined as a state where the time average of measured quantities does not appreciably change if taken over later times.

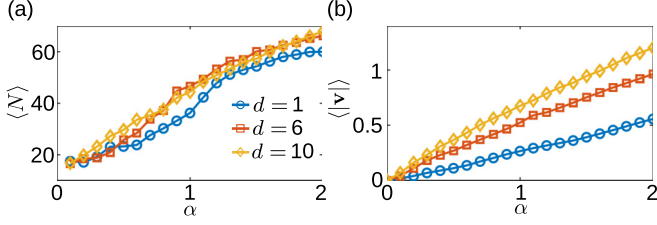


FIG. 2. (a) Average number of topological defects $\langle N \rangle$ versus activity α for simulations with $d = 1$, $d = 6$, and $d = 10$. (b) Average flow speed $\langle |\mathbf{v}| \rangle$ versus α for simulations with $d = 1$, $d = 6$, and $d = 10$.

IV. ACTIVE NEMATIC RATCHET

A schematic of the computational domain with a periodic array of concave triangular shaped obstacles is shown in Fig. 1(a). To understand the effect of obstacle spacing, we fix the distance between obstacle centers at $a = 14$ while we vary the size of the obstacles so that the shortest gap between them, d , changes. Due to the strong planar anchoring, the concave triangles each carry a topological charge (winding number) of $-1/2$. The total topological charge of the system must be 0 due to the periodic boundary conditions, so a defect of charge $+1/2$ must nucleate in the bulk nematic for each obstacle. We show in Fig. 1(b) a time snapshot of the scalar order parameter S and director field \mathbf{n} for a system with $\alpha = 1$ and $d = 4$, while Fig. 1(c) shows the corresponding time snapshot of the velocity and vorticity field. We note that our choice of boundary conditions on the obstacles, namely strong planar anchoring and no-slip velocity, is not identical to the more realistic conditions in the experiments; however, we do not expect our results to qualitatively change if these conditions are relaxed, as long as the anchoring is strong enough to induce topological defects and there is some friction with the obstacles, both of which occur in experiments [16,21].

At $\alpha = 0$, there are no flows in the system and topological defects are pinned to the obstacles. For $\alpha > 0$, topological defects unpin and move while additional defects continuously nucleate and annihilate. For all obstacle gap sizes, we find that the average number of defects in the system and the average magnitude of the flow velocity increases linearly with the activity, as shown in Fig. 2. We compute the number of topological defects using the two-dimensional topological defect density $|D|$ [44,45]:

$$N = \int |\varepsilon_{k\ell} \varepsilon_{\mu\nu} \partial_k Q_{\mu\alpha} \partial_\ell Q_{\nu\alpha}| d\mathbf{r} \quad (8)$$

where ε is the two-dimensional antisymmetric tensor and summation on repeated indices is assumed. The average number of defects, or defect density, and flow velocity are traditional measures of active turbulence in active nematic systems [8,16,46], indicating that the system shares properties with active turbulence for $\alpha > 0$. This differs significantly from our recent study on active nematics in symmetric periodic arrays of obstacles, where multiple phase transitions occurred when varying α [35].

Although the flow measurements in our system are consistent with active turbulence, the detailed nature of the flow differs from traditional active turbulent states, where the

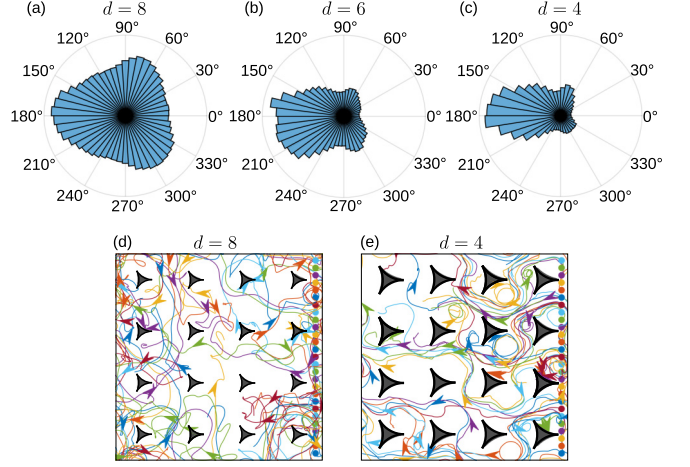


FIG. 3. (a), (b), (c) Distribution of velocity directions $p(\theta_v)$ for varied gap width d at activity $\alpha = 1$. (a) $d = 8$, (b) $d = 6$, (c) $d = 4$. (d), (e) Trajectories of 27 virtual particles over the course of a simulation with (d) $d = 8$ and (e) $d = 4$ at $\alpha = 1$. The dots on the right side indicate the starting positions of the particles.

flow directions are distributed randomly. We find that the flows through our asymmetric obstacle arrays are distributed anisotropically, as illustrated in Figs. 3(a)–3(c), where we plot the distribution of fluid flow directions $p(\theta_v)$ in systems with $\alpha = 1$. When the obstacle gap is large, as shown in Fig. 3(a) for $d = 8$, the flow directions match the threefold symmetry directions of the obstacle surfaces, suggesting that the obstacles are merely locally modulating the flow. As d decreases, however, $p(\theta_v)$ becomes strongly peaked along $\theta_v = \pi$, as shown in Figs. 3(b) and 3(c) for $d = 6$ and $d = 4$, respectively. This indicates the emergence of a directional or rectified flow in the absence of an external drive. To visualize the rectification of the flow, in Figs. 3(d) and 3(e) we plot the trajectories of 27 virtual tracer particles that are initially placed near the right outer boundary of the domain and are advected by the flow over the course of a simulation. In Fig. 3(d), for the wide gap case of $d = 8$ where strong rectification is not present, the tracer particles generally remain close to their starting points and have no coordinated motion. In contrast, for $d = 4$ in Fig. 3(e), the tracer particles tend to travel towards the left side of the domain, as indicated by the appearance of a gradient in the density of the trajectories and regions of aligned flow.

To further quantify the unidirectional flow we measure the space and time averaged x component of the flow velocity $\langle v_x \rangle$. Figure 4(a) shows $\langle v_x \rangle$ versus activity α for a range of d values. When $d \geq 8$, $\langle v_x \rangle \sim 0$ for all α , indicating that there is no net flow in the x direction. For $d \leq 7$, we find that the magnitude of $\langle v_x \rangle$ increases linearly with increasing α . Since the sign of $\langle v_x \rangle$ is negative, this indicates that there is a net flow to the left that becomes greater as the activity increases. That $\langle v_x \rangle$ increases with α even into the large α regime is a surprising result, as active turbulence typically dominates and destroys order in this regime. Indeed, this is the case for symmetric obstacle arrays [35]. Flows tend to move in the negative x direction in this system because they

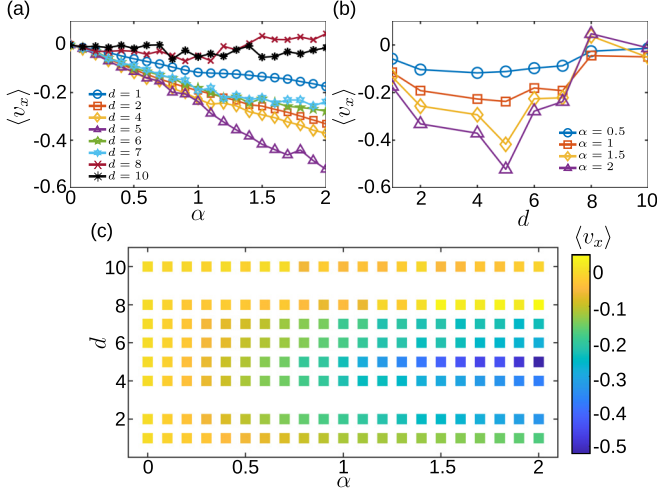


FIG. 4. (a) Average x velocity of the flow field $\langle v_x \rangle$ vs activity α for $d = 1, 2, 4, 5, 6, 7, 8$, and 10 . (b) $\langle v_x \rangle$ vs d for representative α values of $\alpha = 0.5, 1, 1.5$, and 2 . (c) Heat map of $\langle v_x \rangle$ plotted as a function of α vs d .

are easily able to flow from the large gap ends to the small gap ends, but cannot easily move in the other direction as they get trapped against the wide back surface of the triangular obstacles, similar to ratchets observed in self-propelled particle active matter systems [32]. This effect is visualized by the trajectories of virtual tracer particles in Fig. 3(e) where the particles occasionally get stuck in vortices but do not move from the left side of obstacles to the right.

Interestingly, we find the magnitude of $\langle v_x \rangle$ varies non-monotonically with d at fixed α , as illustrated in Fig. 4(b). To identify the overall greatest magnitude of the average flow, we plot a heat map of $\langle v_x \rangle$ as a function of α versus d in Fig. 4(c), and find that the maximum ratchet effect occurs for the largest simulated value of α , $\alpha = 2$, at $d = 5$. As shown in Fig. 2, while the overall flow speed increases with activity, it decreases with decreasing gap size. This is expected as the obstacles are larger for smaller gap sizes, and the no-slip condition on the obstacles yields smaller flow speed overall. We also expect, however, that the ratchet effect is enhanced for smaller gap size, as the spatial region in which flows may reverse is smaller. To further investigate this, we plot $|\langle v_x \rangle / |\mathbf{v}||$, which gives the average ratio of coherent flow in the x direction to total flow speed, versus d in Fig. 5 for $\alpha \in \{0.5, 1, 1.5, 2\}$. As the plot indicates, the maximum ratio of x -direction flow to total flow speed occurs at small gap sizes ($d = 2$) when $\alpha \leq 1$. This indicates that the ratchet effect does indeed increase for smaller gap sizes. However, for larger activities, $\alpha > 1$, we find that the maximum ratio shifts to moderate gap size, $d = 5$, indicating a second potential mechanism for flow speed modulation. We show in the next section that this mechanism is related to the topological defect dynamics in the system, which dominate at large α when defect density is large.

There are previous studies that have shown that breaking rotational symmetry in a circular or annular domain or along a circular inclusion may induce unidirectional azimuthal flows [36,37]. Further, it has been shown in channel geometries for

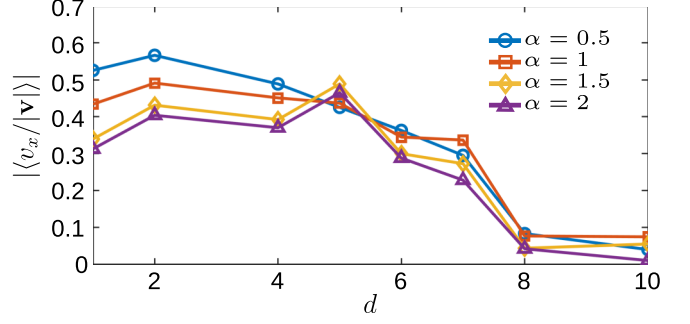


FIG. 5. Average ratio of coherent x -direction flow to total flow speed $|\langle v_x \rangle / |\mathbf{v}||$ versus obstacle gap size d for representative α values of $\alpha = 0.5, 1, 1.5$, and 2 .

small values of the activity that unidirectional flows may occur [4]; however, the flow direction is a spontaneously broken symmetry, and may be in either direction along the channel. Additionally, at higher activities, the emergence of either vortex lattices or active turbulence destroy the unidirectional flow [4,47]. For the triangular obstacles studied here, the direction of the active nematic ratchet flow is set by the asymmetry of the obstacle. To our knowledge, this is the first observation of translational active nematic ratcheting behavior. Further, below a critical gap size, the ratchet effect is robust to activity level and obstacle gap size, indicating that it would not be necessary to extensively tune the system parameters to obtain ratcheting motion for microfluidic applications.

V. DEFECT DYNAMICS

To better understand the maximal ratchet behavior at high activities, we investigate the topological defect dynamics for varying obstacle size and find that there is a transition in defect behavior. We first measure the distribution of defect velocity directions by measuring the topological current [45,48]

$$J_i = \epsilon_{ik} \epsilon_{\mu\nu} \partial_i Q_{\mu\alpha} \partial_k Q_{\nu\alpha}, \quad (9)$$

which is proportional to topological defect velocities at the location of defects. For large d , the plot of the distribution $p(\theta_+)$ of the velocities of $+1/2$ winding defects in Fig. 6(a) for $d = 8$ and $\alpha = 1.5$ indicates that the $+1/2$ winding defects move in the same direction as the flow [compare to Fig. 3(a)]. At the same time, Fig. 6(d) indicates that the $-1/2$ winding defect velocity distribution, $p(\theta_-)$, is much more isotropic. As the gap size decreases, the ratchet effect emerges and the net flow velocity is primarily along the $-x$ direction, but for $d = 5$ the $+1/2$ defect velocities break the up-down symmetry of the domain, as shown by the plot of $p(\theta_+)$ in Fig. 6(b). In this intermediate regime, the $-1/2$ defects also break up-down symmetry and tend to move in the direction opposite to the primary flow direction of the $+1/2$ defects, as illustrated by the plot of $p(\theta_-)$ in Fig. 6(e). We note that if we perform additional simulations with differing random initial conditions we still find the symmetry breaking along the y -direction to varying degrees, and approximately half of the realizations break the symmetry in the $\pm y$ direction, indicating a spontaneously broken symmetry that depends on the first few defect nucleations. In the limit of small d , shown

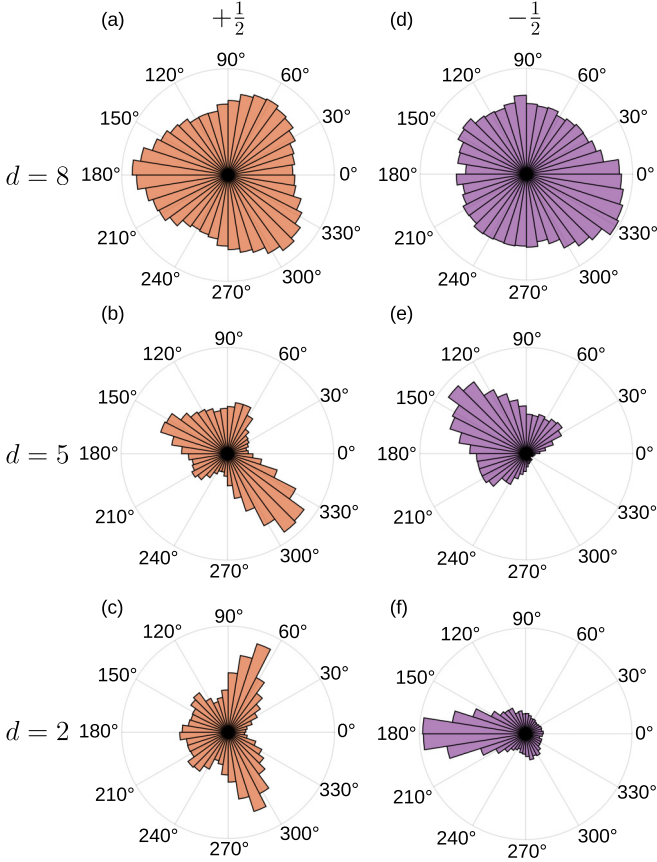


FIG. 6. Defect velocity direction distributions (a)–(c) $p(\theta_+)$ for $+1/2$ defects and (d)–(f) $p(\theta_-)$ for $-1/2$ defects at $\alpha = 1.5$ for (a), (d) $d = 8$, (b), (e) $d = 5$, and (c), (f) $d = 2$.

in the plots of $p(\theta_+)$ and $p(\theta_-)$ in Figs. 6(c) and 6(f) at $d = 2$, the $+1/2$ defects tend to move either up or down with equal frequency, restoring the up-down symmetry of the domain, while the $-1/2$ defects primarily move to the left, in the direction of the ratcheting flow. We note that in this regime the $+1/2$ defects tend to move transverse to the fluid flow direction.

To better understand the defect dynamics, in Figs. 7(a)–7(c) we construct defect density plots N/N_{\max} as a function of position relative to the obstacle for the $+1/2$ defects at different values of d , and show the corresponding N/N_{\max} plots for the $-1/2$ defects in Figs. 7(d)–7(f). Here, we first accumulate N , the local defect density around each obstacle, on a grid surrounding the obstacle during the entire simulation. We then sum this quantity over all obstacles and normalize it by the maximum value N_{\max} on the grid. For $d = 8$ in Figs. 7(a) and 7(d), both the positive and negative defects are distributed throughout the interobstacle region, with peak values of N/N_{\max} appearing close to the obstacle for the $+1/2$ defects. Thus, for large gap sizes, defects of both signs are freely moving in the domain, but the $+1/2$ defects can become briefly pinned by the obstacles. We note that the defect densities we measure for large gap sizes (small obstacles) are similar to those measured in a system with similarly shaped obstacles [21]. The densities are also similar to those measured in Ref. [49] for the pair distribution function around

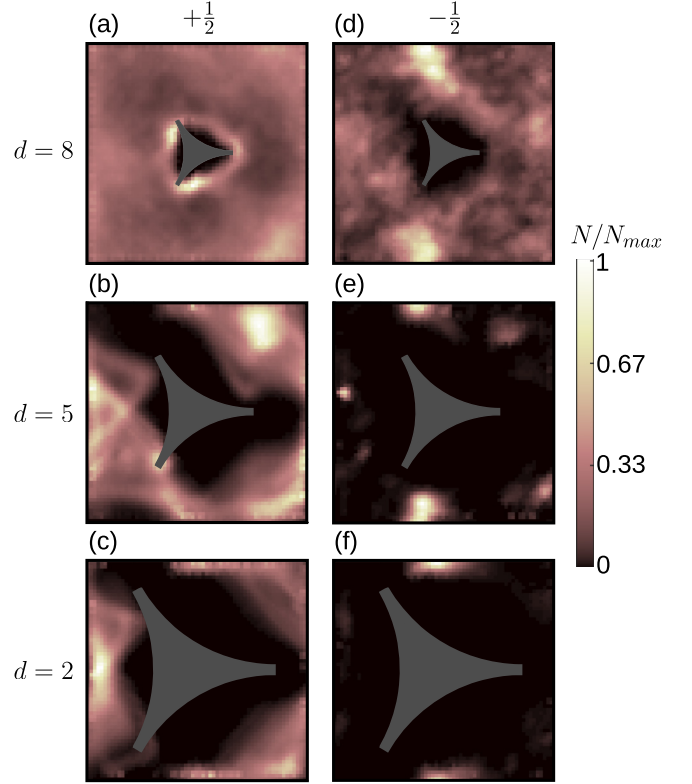


FIG. 7. Distribution of defects around obstacles. The distribution around each obstacle in a simulation is computed and then all are added together to form the plots. (a)–(c) Distribution of $+1/2$ defects and (d)–(f) distribution of $-1/2$ defects for simulations with (a), (d) $d = 8$, (b), (e) $d = 5$, (c), (f) $d = 2$ and $\alpha = 1.5$.

defects in active turbulence, and we expect the densities to match as the obstacles are smaller. For $d = 5$ in Figs. 7(b) and 7(e), N/N_{\max} for the $+1/2$ defects breaks the up-down symmetry of the obstacle and is largest along a line in interstitial space connecting the left and right sides of the obstacle, indicating that the defects are flowing horizontally. Further, there are no longer strong peaks in N/N_{\max} near the obstacle, indicating that the $+1/2$ defects no longer become pinned. At the same time, the distribution of negative defects becomes highly concentrated in the region between the upper and lower sides of the obstacles, indicating defect localization in this area. At $d = 2$ in Figs. 6(c) and 7(f), N/N_{\max} for positive defects mirrors the symmetry of the obstacles but drops nearly to zero partway across the region connecting the left and right sides of the obstacles, indicating that $+1/2$ defects are no longer flowing horizontally. Meanwhile, the $-1/2$ defects become even more strongly localized in the region between obstacles.

We find that at large gap sizes, the motion of the defects tends to mirror the flow of the system, but that the defects may become pinned for a period of time, reducing their flow speed. As the gap size decreases, the likelihood of pinning diminishes and the defects can move more freely. At a critical gap size of $d = 5$, the negative defects become strongly localized in the vertical gap between obstacles. At first this allows the positive defects to travel more efficiently in the $-x$ direction by skirting the negative defects, but as the gap

size diminishes further, the positive defects begin to annihilate with the negative defects and the x -direction flow is lost. Instead, the $+1/2$ defects begin to travel transverse to the flow in lanes along the y direction, forming a smectic-like defect state. In the Supplemental Material, Movies 1–3, we show the nematic configuration and flow velocities for simulations in these three regimes [50].

Since we find maximal $-x$ direction flow at $d = 5$ for all values of α , the maximum does not result from a commensuration effect between d and the active length scale $\xi_a \propto 1/\sqrt{\alpha}$. Instead, the commensuration occurs between d and the characteristic size of topological defects ξ_d , which we hold fixed in this study. It appears when d reaches a length for which $-1/2$ defects become localized between the obstacles, enhancing the overall flow. In particular, this has the effect of further enhancing the active nematic flow ratchet behavior for $d = 5$ while diminishing the flows for other gap sizes at high activities when the defect density is large and the defect dynamics dominate the active flows.

VI. CONCLUSION

We showed numerically that a periodic array of asymmetric obstacles can produce translational ratchet flows in an active nematic. As the gap distance between obstacles decreases, the flow velocity directions become peaked along the asymmetry direction, but the average flow velocity

varies nonmonotonically. The obstacle asymmetry induces a translational active nematic ratchet that has not been described previously. The ratcheting effect is robust over a large range of obstacle gap sizes and activity levels. We also observed a transition in defect dynamics that is correlated with the flow speed non-monotonicity. Positive winding defects follow the fluid flow for large gap sizes, while for small gap sizes, pinned negative defects inhibit the movement of positive defects along the flow and cause the positive defects to travel transverse to the flow.

This work opens a variety of future directions for steering or patterning active nematic flows and defect structures using ratchet geometries. Such effects have potential microfluidic applications, including logic gate design [12] or the creation of complex patterns [51]. It would be interesting to explore other asymmetric obstacle geometries or lattice arrangements. Different obstacle geometries may produce distinct topological defect arrangements, while different lattices may generate novel flow patterns.

ACKNOWLEDGMENTS

This work was supported by the U.S. Department of Energy through the Los Alamos National Laboratory. Los Alamos National Laboratory is operated by Triad National Security, LLC, for the National Nuclear Security Administration of the U.S. Department of Energy (Contract No. 89233218CNA000001).

-
- [1] M. C. Marchetti, J. F. Joanny, S. Ramaswamy, T. B. Liverpool, J. Prost, M. Rao, and R. A. Simha, Hydrodynamics of soft active matter, *Rev. Mod. Phys.* **85**, 1143 (2013).
 - [2] A. Doostmohammadi, J. Ignés-Mullol, J. M. Yeomans, and F. Sagués, Active nematics, *Nat. Commun.* **9**, 3246 (2018).
 - [3] T. Sanchez, D. T. N. Chen, S. J. DeCamp, M. Heymann, and Z. Dogic, Spontaneous motion in hierarchically assembled active matter, *Nature (London)* **491**, 431 (2012).
 - [4] A. Doostmohammadi, T. N. Shendruk, K. Thijssen, and J. M. Yeomans, Onset of meso-scale turbulence in active nematics, *Nat. Commun.* **8**, 15326 (2017).
 - [5] R. Alert, J.-F. Joanny, and J. Casademunt, Universal scaling of active nematic turbulence, *Nat. Phys.* **16**, 682 (2020).
 - [6] L. N. Carenza, L. Biferale, and G. Gonnella, Cascade or not cascade? Energy transfer and elastic effects in active nematics, *Europhys. Lett.* **132**, 44003 (2020).
 - [7] L. Giomi, M. J. Bowick, P. Mishra, R. Sknepnek, and M. C. Marchetti, Defect dynamics in active nematics, *Phil. Trans. R. Soc. A* **372**, 20130365 (2014).
 - [8] S. J. DeCamp, G. S. Redner, A. Baskaran, M. F. Hagan, and Z. Dogic, Orientational order of motile defects in active nematics, *Nat. Mater.* **14**, 1110 (2015).
 - [9] S. Shankar and M. C. Marchetti, Hydrodynamics of active defects: From order to chaos to defect ordering, *Phys. Rev. X* **9**, 041047 (2019).
 - [10] L. Angheluta, Z. Chen, M. C. Marchetti, and M. J. Bowick, The role of fluid flow in the dynamics of active nematic defects, *New J. Phys.* **23**, 033009 (2021).
 - [11] J. Rønning, C. M. Marchetti, M. J. Bowick, and L. Angheluta, Flow around topological defects in active nematic films, *Proc. R. Soc. A: Math. Phys. Eng. Sci.* **478**, 20210879 (2022).
 - [12] F. G. Woodhouse and J. Dunkel, Active matter logic for autonomous microfluidics, *Nat. Commun.* **8**, 15169 (2017).
 - [13] P. Guillamat, J. Ignés-Mullol, and F. Sagués, Control of active liquid crystals with a magnetic field, *Proc. Natl. Acad. Sci. USA* **113**, 5498 (2016).
 - [14] P. Guillamat, J. Ignés-Mullol, S. Shankar, M. C. Marchetti, and F. Sagués, Probing the shear viscosity of an active nematic film, *Phys. Rev. E* **94**, 060602(R) (2016).
 - [15] T. N. Shendruk, A. Doostmohammadi, K. Thijssen, and J. M. Yeomans, Dancing disclinations in confined active nematics, *Soft Matter* **13**, 3853 (2017).
 - [16] A. Opatthalage, M. M. Norton, M. P. N. Juniper, B. Langeslay, S. A. Aghvami, S. Fraden, and Z. Dogic, Self-organized dynamics and the transition to turbulence of confined active nematics, *Proc. Natl. Acad. Sci. USA* **116**, 4788 (2019).
 - [17] K. Thijssen, L. Metselaar, J. M. Yeomans, and A. Doostmohammadi, Active nematics with anisotropic friction: the decisive role of the flow aligning parameter, *Soft Matter* **16**, 2065 (2020).
 - [18] K. Thijssen, D. A. Khaladj, S. A. Aghvami, M. A. Gharbi, S. Fraden, J. M. Yeomans, L. S. Hirst, and T. N. Shendruk, Submersed micropatterned structures control active nematic flow, topology, and concentration, *Proc. Natl. Acad. Sci. USA* **118**, e2106038118 (2021).
 - [19] R. Zhang, A. Mozaffari, and J. J. de Pablo, Logic operations with active topological defects, *Sci. Adv.* **8**, eabg9060 (2022).

- [20] Z. Zarei, J. Berezney, A. Hensley, L. Lemma, N. Senbil, Z. Dogic, and S. Fraden, Light-activated microtubule-based two-dimensional active nematic, *Soft Matter* **19**, 6691 (2023).
- [21] N. Figueroa-Morales, M. M. Genkin, A. Sokolov, and I. S. Aranson, Non-symmetric pinning of topological defects in living liquid crystals, *Commun. Phys.* **5**, 301 (2022).
- [22] I. Vélez-Cerón, P. Guillamat, F. Sagués, and J. Ignés-Mullol, Probing active nematics with in situ microfabricated elastic inclusions, *Proc. Natl. Acad. Sci. USA* **121**, e2312494121 (2024).
- [23] M. O. Magnasco, Forced thermal ratchets, *Phys. Rev. Lett.* **71**, 1477 (1993).
- [24] R. D. Astumian and M. Bier, Fluctuation driven ratchets: Molecular motors, *Phys. Rev. Lett.* **72**, 1766 (1994).
- [25] R. Bartussek, P. Hänggi, and J. G. Kissner, Periodically rocked thermal ratchets, *Europhys. Lett.* **28**, 459 (1994).
- [26] P. Reimann, Brownian motors: noisy transport far from equilibrium, *Phys. Rep.* **361**, 57 (2002).
- [27] J. Rousselet, L. Salome, A. Ajdari, and J. Prost, Directional motion of Brownian particles induced by a periodic asymmetric potential, *Nature (London)* **370**, 446 (1994).
- [28] A. V. Arzola, K. Volke-Sepúlveda, and J. L. Mateos, Experimental control of transport and current reversals in a deterministic optical rocking ratchet, *Phys. Rev. Lett.* **106**, 168104 (2011).
- [29] C. S. Lee, B. Jankó, I. Derényi, and A. L. Barabási, Reducing vortex density in superconductors using the ‘ratchet effect’, *Nature (London)* **400**, 337 (1999).
- [30] C. C. de Souza Silva, J. V. de Vondel, M. Morelle, and V. V. Moshchalkov, Controlled multiple reversals of a ratchet effect, *Nature (London)* **440**, 651 (2006).
- [31] C. Bechinger, R. Di Leonardo, H. Löwen, C. Reichhardt, G. Volpe, and G. Volpe, Active particles in complex and crowded environments, *Rev. Mod. Phys.* **88**, 045006 (2016).
- [32] C. J. O. Reichhardt and C. Reichhardt, Ratchet effects in active matter systems, *Annu. Rev. Condens. Matter Phys.* **8**, 51 (2017).
- [33] P. Galajda, J. Keymer, P. Chaikin, and R. Austin, A wall of funnels concentrates swimming bacteria, *J. Bacteriol.* **189**, 8704 (2007).
- [34] N. Nikola, A. P. Solon, Y. Kafri, M. Kardar, J. Tailleur, and R. Voituriez, Active particles with soft and curved walls: Equation of state, ratchets, and instabilities, *Phys. Rev. Lett.* **117**, 098001 (2016).
- [35] C. D. Schimming, C. J. O. Reichhardt, and C. Reichhardt, Vortex lattices in active nematics with periodic obstacle arrays, *Phys. Rev. Lett.* **132**, 018301 (2024).
- [36] K.-T. Wu, J. B. Hishamunda, D. T. N. Chen, S. J. DeCamp, Y.-W. Chang, A. Fernández-Nieves, S. Fraden, and Z. Dogic, Transition from turbulent to coherent flows in confined three-dimensional active fluids, *Science* **355**, eaal1979 (2017).
- [37] S. Ray, J. Zhang, and Z. Dogic, Rectified rotational dynamics of mobile inclusions in two-dimensional active nematics, *Phys. Rev. Lett.* **130**, 238301 (2023).
- [38] D. Marenduzzo, E. Orlandini, M. E. Cates, and J. M. Yeomans, Steady-state hydrodynamic instabilities of active liquid crystals: Hybrid lattice boltzmann simulations, *Phys. Rev. E* **76**, 031921 (2007).
- [39] A. N. Beris and B. J. Edwards, *Thermodynamics of Flowing Systems* (Oxford University Press, Oxford, 1994).
- [40] E. J. Hemingway, P. Mishra, M. C. Marchetti, and S. M. Fielding, Correlation lengths in hydrodynamic models of active nematics, *Soft Matter* **12**, 7943 (2016).
- [41] S. W. Walker, Tetrahedralization of isosurfaces with guaranteed-quality by edge rearrangement (TIGER), *SIAM J. Sci. Comput.* **35**, A294 (2013).
- [42] S. W. Walker, FELICITY: A MATLAB/C++ toolbox for developing finite element methods and simulation modeling, *SIAM J. Sci. Comput.* **40**, C234 (2018).
- [43] F. M. Leslie, Some constitutive equations for anisotropic fluids, *J. Mech. Appl. Math.* **19**, 357 (1966).
- [44] M. L. Blow, S. P. Thampi, and J. M. Yeomans, Biphasic, lyotropic, active nematics, *Phys. Rev. Lett.* **113**, 248303 (2014).
- [45] C. D. Schimming and J. Viñals, Singularity identification for the characterization of topology, geometry, and motion of nematic disclination lines, *Soft Matter* **18**, 2234 (2022).
- [46] L. M. Lemma, S. J. DeCamp, Z. You, L. Giomi, and Z. Dogic, Statistical properties of autonomous flows in 2D active nematics, *Soft Matter* **15**, 3264 (2019).
- [47] J. Hardouin, R. Hughes, A. Doostmohammadi, J. Laurent, T. Lopez-Leon, J. M. Yeomans, J. Ignés-Mullol, and S. Francese, Reconfigurable flows and defect landscape of confined active nematics, *Commun. Phys.* **2**, 121 (2019).
- [48] C. D. Schimming and J. Viñals, Kinematics and dynamics of disclination lines in three-dimensional nematics, *Proc. R. Soc. A* **479**, 20230042 (2023).
- [49] K. Thijssen, M. R. Nejad, and J. M. Yeomans, Role of friction in multidefect ordering, *Phys. Rev. Lett.* **125**, 218004 (2020).
- [50] See Supplemental Material at <http://link.aps.org/supplemental/10.1103/PhysRevE.109.064602> for supplementary videos.
- [51] C. Jorge, A. Chardac, A. Poncet, and D. Bartolo, Active hydraulics laws from frustration principles, *Nat. Phys.* **20**, 303 (2024).